

Roles of nonlocal electron-phonon coupling on the electrical conductivity and Seebeck coefficient: A time-dependent DMRG study

Yufei Ge¹, Weitang Li², Jiajun Ren,³ and Zhigang Shuai^{4,*}

¹MOE Key Laboratory on Organic OptoElectronics and Molecular Engineering, Department of Chemistry, Tsinghua University, 100084 Beijing, China

²Tencent Quantum Lab, Tencent, Shenzhen, 518057 Guangdong, China

³MOE Key Laboratory of Theoretical and Computational Photochemistry, College of Chemistry, Beijing Normal University, 100875 Beijing, People's Republic of China

⁴School of Science and Engineering, The Chinese University of Hong Kong, Shenzhen, 518172 Guangdong, China



(Received 19 December 2023; revised 1 June 2024; accepted 17 June 2024; published 3 July 2024)

Organic molecular materials are potential high-performance thermoelectric materials. Theoretical understanding of thermoelectric conversion in organic materials is essential for rational molecular design for efficient energy conversion materials. In organic materials, nonlocal electron-phonon coupling plays a vital role in charge transport and leads to complex transport mechanisms, including hopping, phonon assisted, band, and transient localization. In this work, based on the time-dependent density matrix renormalization group method, we look at the role of nonlocal electron-phonon coupling on the thermoelectric conversion in organic systems described by the Holstein-Peierls model. We calculate the current-current correlation and the heat current-current correlation functions. We find that (i) nonlocal electron-phonon coupling has a very weak influence on the Seebeck coefficient because of the cancellation between the heat current-current correlation function and the current-current correlation function, but it has a strong influence on the conductivity through dynamic disorders; and (ii) doping concentration has a strong influence on both the conductivity and Seebeck coefficient, and the optimal doping ratio to reach the highest power factor is 3%–10% fillings when the Holstein-Peierls model is valid. These findings suggest that we can design organic materials with higher power factors by first enhancing mobility through rational design, and then searching for the optimal doping ratio.

DOI: [10.1103/PhysRevB.110.035201](https://doi.org/10.1103/PhysRevB.110.035201)

I. INTRODUCTION

Organic materials hold immense potential for next-generation thermoelectric devices [1–7], prompting significant research efforts towards designing high-performance organic thermoelectric materials over the past decade [5,8–11]. The figure of merit (ZT) of organic materials at room temperature has been improved by more than one order of magnitude in the past decades [12–16]. The ZT value, which measures the performance of thermoelectric materials, is defined as $ZT = \frac{\alpha^2 \sigma T}{\kappa_e + \kappa_L}$, where α , σ , T , and κ_e (κ_L) represent the Seebeck coefficient, electrical conductivity, temperature, and electrical and (lattice) thermal conductivity. The rapid improvement in ZT can be attributed to the ingenious concept named “electron crystal, phonon glass” [6], which emphasizes the independent control of the lattice thermal conductivity and the electrical conductivity. Along this line, numerous techniques have been proposed [17]. However, the ZT values of organic materials are still low, which limits application. One restriction is that the conductivity and Seebeck coefficient usually behave oppositely, which limits the enhancement of the power factor ($PF = \alpha^2 \sigma$) and ZT value.

Essentially, the Seebeck coefficient represents the “transport entropy,” which is the entropy carried by the unit charge carrier in charge transport [18,19]. Therefore, to enhance the thermoelectric performance further, it is necessary to interpret the charge carriers’ thermoelectric transport process comprehensively. Obviously, electron-phonon coupling plays a vital role in thermoelectric transport. Generally speaking, electron-phonon coupling can be attributed to two types: local electron-phonon coupling, originating from intramolecular vibration and nonlocal electron-phonon coupling comes from intermolecular vibration. Previous studies have systematically revealed the effect of local electron-phonon coupling which decreases the conductivity and enhances the Seebeck coefficient by bandwidth narrowing effect [20–22]. Meanwhile, nonlocal electron-phonon coupling which can lead to the formation of solitons, polarons, and bipolarons [23,24], influencing charge transport [25,26] and exciton dynamic [27,28] and spectral properties [29] significantly, has not been fully [30] studied in thermoelectric transport.

According to previous research, nonlocal electron-phonon coupling introduces nonlocal dynamic disorder and involves various transport regimes, including (i) a hopping regime [11,31–34] where charge carriers are localized at one molecule because of strong local electron-phonon coupling, and “hop” from one molecule to another, (ii) a

*Contact author: shuaizhigang@cuhk.edu.cn

phonon-assisted regime [35,36] where there exists a large thermal fluctuation of transfer integrals induced by nonlocal electron-phonon coupling, which enhances mobility, (iii) a band regime [37–39] where charge carriers move “wavelike” and are scattered by nonlocal phonons and impurities, (iv) a transient localization regime [40–42] where charge carriers are time-dependently localized at several molecules by the motion of molecules (dynamic disorder), and (v) an intermediate regime [30] which belongs to none of the regimes mentioned above.

The involved complex transport regimes hindered the comprehensive understanding of nonlocal electron-phonon coupling on thermoelectric transport for a long time because of the lack of a numerically exact simulation method [25]. Fortunately, the time-dependent density matrix renormalization group [43–45] (TD-DMRG) has the potential to overcome the difficulty in simulation [30,46], and in our previous work the computational methods for calculating the conductivity and Seebeck coefficient by TD-DMRG have been developed, which are both valid and numerically exact [22].

In this work, we will adopt the TD-DMRG to investigate thermoelectric transport in organic materials and reveal the influence of nonlocal electron-phonon coupling in different charge transport regimes.

II. MODEL AND COMPUTATIONAL APPROACH

The Holstein-Peierls model [23,47] captures the effect of local and nonlocal electron-phonon coupling in organic materials [48]. In this work, we consider N molecules in a one-dimensional chain with lattice constant Ω and each molecule contributes one molecular orbital (LUMO or HOMO corresponding to n -type or p -type doping) to the thermoelectric transport process. With the periodic boundary condition, the Hamiltonian contains the following five parts:

$$\hat{H} = \hat{H}_e + \hat{H}_{e\text{-ph1}} + \hat{H}_{e\text{-ph2}} + \hat{H}_{\text{ph1}} + \hat{H}_{\text{ph2}}. \quad (1)$$

Here, the electron part reads

$$\hat{H}_e = \sum_j \epsilon_j \hat{a}_j^\dagger \hat{a}_j + \sum_j \tau_{j,j+1} (\hat{a}_{j+1}^\dagger \hat{a}_j + \hat{a}_j^\dagger \hat{a}_{j+1}). \quad (2)$$

In the electron part, \hat{a}_j^\dagger and \hat{a}_j are the creation and annihilation operators, respectively, of the j th molecule’s orbital. Considering the tradition of the DMRG, we denote it as “site j ” below for brevity. ϵ_j and $\tau_{j,j+1}$ are the orbital energy at site j and the transfer integral between sites j and $j+1$, respectively. For simplicity, we set $\epsilon_j = 0$ and $\tau_{j,j+1} = \tau$.

The Holstein model captures the effect of intramolecular electron-vibration coupling (i.e., local coupling), including the bandwidth narrowing effect and reorganization energy [21,49,50]. $\hat{H}_{e\text{-ph1}}$ and \hat{H}_{ph1} correspond to the Holstein model. Here, the local electron-phonon coupling term is

$$\hat{H}_{e\text{-ph1}} = \sum_{j,n} \hbar g_{H,n} \omega_{H,n} (\hat{b}_{jn}^\dagger + \hat{b}_{jn}) \hat{a}_j^\dagger \hat{a}_j \quad (3)$$

and the local phonon energy term is

$$\hat{H}_{\text{ph1}} = \sum_{j,n} \hbar \omega_{H,n} \left(\hat{b}_{jn}^\dagger \hat{b}_{jn} + \frac{1}{2} \right). \quad (4)$$

\hat{b}_{jn}^\dagger and \hat{b}_{jn} are the creation and annihilation operators, respectively, of the phonons corresponding to the n th vibration mode at site j . $\omega_{H,n}$ and $g_{H,n}$ are the phonon frequency and the electron-phonon coupling constant of the n th intramolecular vibration mode. The reorganization energy is defined as $\lambda = \sum_n g_{H,n}^2 \omega_{H,n}$, which represents the strength of local electron-phonon coupling. For simplicity, we use four modes, $\omega_H = 40, 120, 200,$ and 280 meV and $g_H = 1.247, 0.645, 0.2311,$ and 0.0792 .

The Peierls model captures the effect of intermolecular electron-vibration coupling (i.e., nonlocal coupling), leading to thermal fluctuation of transfer integrals [25]. $\hat{H}_{e\text{-ph2}}$ and \hat{H}_{ph2} correspond to the Peierls model. Here, the nonlocal electron-phonon coupling term is

$$\hat{H}_{e\text{-ph2}} = \sum_j \hbar g_P \omega_P (\hat{c}_j^\dagger + \hat{c}_j) (\hat{a}_j^\dagger \hat{a}_{j+1} + \hat{a}_{j+1}^\dagger \hat{a}_j) \quad (5)$$

and the nonlocal phonon energy is

$$\hat{H}_{\text{ph2}} = \sum_j \hbar \omega_P \left(\hat{c}_j^\dagger \hat{c}_j + \frac{1}{2} \right). \quad (6)$$

Here, \hat{c}_j^\dagger and \hat{c}_j are the creation and annihilation operators, respectively, of the phonons corresponding to the intermolecular vibration between site j and site $j+1$. ω_P and g_P are the vibration frequency and coupling constant of the intermolecular vibration mode. For simplicity, one intermolecular vibration mode $\omega_P = 10$ meV is adopted [48,51]. Thermal fluctuation of transfer integral $\Delta V = \sqrt{\langle \tau^2 \rangle} - \langle \tau \rangle^2$ reflects the dynamic disorder introduced by temperature and nonlocal coupling. ΔV is related to nonlocal electron-phonon coupling as presented below [52,53]:

$$\Delta V = g_P \omega_P \sqrt{\coth \frac{\omega_P}{2k_B T}}. \quad (7)$$

In our program, g_P is used as the input parameter for calculation, while g_P is more abstract than ΔV . Therefore, ΔV is adopted to distinguish different transport regimes [use Eq. (7)], and we will use ΔV in Figs. 2 and 3. Considering ΔV also changes with temperature, g_P is adopted in other cases.

The conductivity σ and Seebeck coefficient α are calculated via the Kubo formula [20,21]:

$$\sigma = \frac{1}{k_B T V} \int_0^{+\infty} \text{Re } C_1(t) dt, \quad \alpha = \frac{1}{T} \frac{\int_0^{+\infty} \text{Re } C_2(t) dt}{\int_0^{+\infty} \text{Re } C_1(t) dt}, \quad (8)$$

where V is the volume of the unit cell, T is temperature, k_B is the Boltzmann constant, and the current-current correlation function $C_1(t)$ and heat current-current correlation function $C_2(t)$ are defined as below [54]:

$$\begin{aligned} C_1(t) &= \text{Tr}[\hat{\rho}_0 e^{i\hat{H}t/\hbar} \hat{J}_e e^{-i\hat{H}t/\hbar} \hat{J}_e], \\ C_2(t) &= \text{Tr}[\hat{\rho}_0 e^{i\hat{H}t/\hbar} \hat{J}_Q e^{-i\hat{H}t/\hbar} \hat{J}_e]. \end{aligned} \quad (9)$$

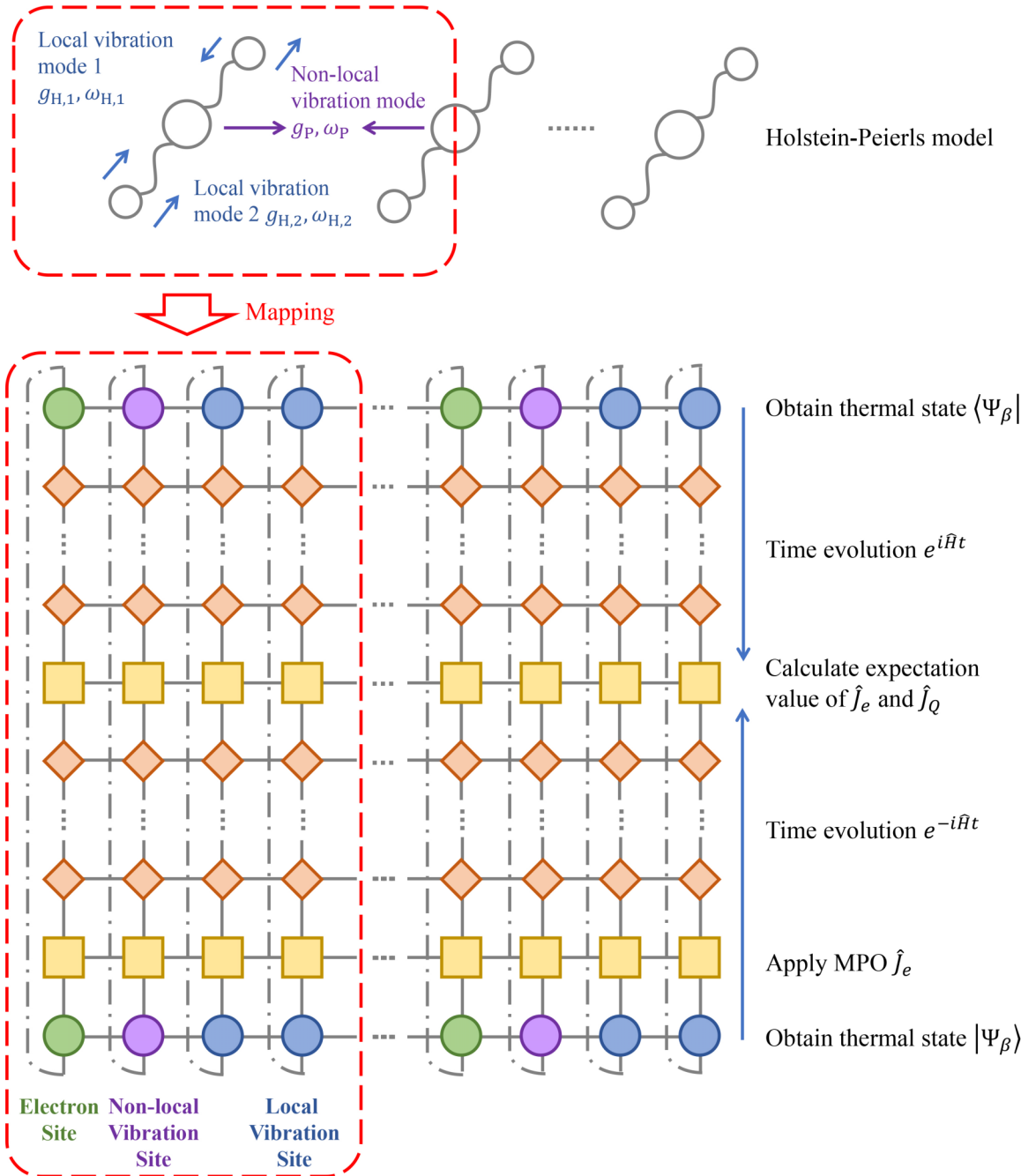


FIG. 1. Schematic diagram of the numerical calculation progress. Here, we map the Holstein-Peierls model to the tensors in the DMRG calculation. If we consider two local vibration modes in each molecular and nearest-neighbor nonlocal vibration (red dotted box), we can align the tensors (sites) of electrons, nonlocal vibrations, and local vibrations as presented above.

Here, \hat{J}_e represents the electrical current operator:

$$\hat{J}_e = -\frac{i}{\hbar}e\Omega \sum_j \hat{T}_{j,j+1}(\hat{a}_{j+1}^\dagger \hat{a}_j - \hat{a}_j^\dagger \hat{a}_{j+1}). \quad (10)$$

\hat{J}_Q represents the heat current operator:

$$\hat{J}_Q = \hat{J}_Q^I + \hat{J}_Q^{II} + \hat{J}_Q^{III}, \quad (11)$$

$$\hat{J}_Q^I = -\frac{i}{\hbar}\Omega \sum_j \hat{T}_{j,j+1} \hat{T}_{j+1,j+2}(\hat{a}_{j+2}^\dagger \hat{a}_j - \hat{a}_j^\dagger \hat{a}_{j+2}), \quad (12)$$

$$\hat{J}_Q^{II} = -\frac{i}{\hbar}\Omega \sum_j \left[\frac{1}{2}(\hat{E}_j + \hat{E}_{j+1}) - \mu \right] \times \hat{T}_{j,j+1}(\hat{a}_{j+1}^\dagger \hat{a}_j - \hat{a}_j^\dagger \hat{a}_{j+1}), \quad (13)$$

$$\hat{J}_Q^{III} = \frac{i}{2\hbar}\Omega \sum_j \hbar^2 g_P \omega_P^2 (\hat{c}_j^\dagger - \hat{c}_j)(\hat{a}_{j+1}^\dagger \hat{a}_j + \hat{a}_j^\dagger \hat{a}_{j+1}). \quad (14)$$

Here, \hat{J}_Q^I , \hat{J}_Q^{II} , and \hat{J}_Q^{III} represent the heat current originating from the electron's kinetic energy, the electron's potential

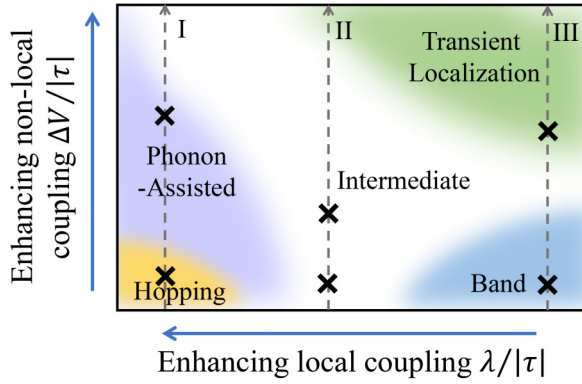


FIG. 2. Five transport regimes in organic materials. The yellow part is the hopping regime, where $|\tau| \ll \lambda$ and $\Delta V \ll |\tau|$; the purple part is the phonon-assisted regime, where $|\tau| \ll \lambda$ and ΔV is comparable to or larger than $|\tau|$; the blue part is the band regime, where $|\tau| \gg \lambda$ and $\Delta V \ll |\tau|$; the green part is the transient localization regime, where $|\tau| \gg \lambda$ and ΔV is comparable to or larger than $|\tau|$; the white part is the intermediate regime, where $|\tau| \sim \lambda$ and $\Delta V \sim |\tau|$. The gray dashed lines (I), (II), and (III) correspond to the parameter selection in Fig. 3. The black crosses correspond to the representative parameters of five transport regimes, which are adopted in Figs. 4–6.

energy, and intermolecular vibration. And \hat{E}_j is the on-site energy operator corrected by the local phonon and $\hat{T}_{j,j+1}$ is the transfer integral operator corrected by the nonlocal phonon:

$$\hat{E}_j = \epsilon_j + \sum_n \hbar g_{H,n} \omega_{H,n} (\hat{b}_{jn}^\dagger + \hat{b}_{jn}), \quad (15)$$

$$\hat{T}_{j,j+1} = \tau_{j,j+1} + \hbar g_{P,\omega_P} (\hat{c}_j^\dagger + \hat{c}_j). \quad (16)$$

The thermoelectric transport process is understood under the grand canonical ensemble and the density operator is

$$\hat{\rho}_0 = \frac{1}{Z} e^{-\beta(\hat{H} - \mu \hat{N}_e)}. \quad (17)$$

Here, the partition function is $Z = \text{Tr}[e^{-\beta(\hat{H} - \mu \hat{N}_e)}]$ and the electron number operator is $\hat{N}_e = \sum_j \hat{a}_j^\dagger \hat{a}_j$. The doping ratio is defined as $c = \text{Tr}[\hat{\rho}_0 \hat{N}_e] / N$. It seems that we can use the particle number conservation for efficient calculation, while the grand canonical ensemble also performs much better in changing the doping ratio continuously, especially when N is small. In addition, we set the lattice constant as $\Omega = 10$ a.u., and the temperature as $T = 300$ K.

The numerical calculation is carried out by transforming Eq. (9) into

$$C_1(t) = \langle \Psi_\beta | e^{i\hat{H}t/\hbar} \hat{J}_e e^{-i\hat{H}t/\hbar} \hat{J}_e | \Psi_\beta \rangle, \quad (18)$$

$$C_2(t) = \langle \Psi_\beta | e^{i\hat{H}t/\hbar} \hat{J}_Q e^{-i\hat{H}t/\hbar} \hat{J}_e | \Psi_\beta \rangle.$$

Here, $|\Psi_\beta\rangle$ is the thermal state obtained by a purification method [44]. As presented in Fig. 1, the electron sites and phonon sites of molecules are mapped to a one-dimensional chain. The green circles, purple circles, and blue circles represent the tensors of thermal states $|\Psi_\beta\rangle$ and $\langle\Psi_\beta|$, corresponding to the electron sites, nonlocal vibration sites, and local vibration sites. Note that the electron sites are

represented by spin basis after Jordan-Wigner transformation. Then, matrix product operator \hat{J}_e is applied to $|\Psi_\beta\rangle$. The orange diamonds represent the time evolution of $\hat{J}_e |\Psi_\beta\rangle$ and $\langle\Psi_\beta|$, where a time-dependent variational principle with a projector-splitting algorithm (TDVP-PS) is adopted [45]. Finally, correlation functions $C_1(t)$ and $C_2(t)$ are obtained by calculating the expectation value of \hat{J}_e and \hat{J}_Q (yellow squares). The sequence of the algorithm is indicated by the blue arrows in Fig. 1. The details of the parameter selections are presented in Appendix A.

III. RESULTS AND DISCUSSIONS

As mentioned above, the effect of nonlocal electron-phonon coupling should be studied across five different regimes [30]. The five regimes are hopping regime, phonon-assisted regime, band regime, transient localization regime, and intermediate regime, as presented in Fig. 2.

First, we study the influence of nonlocal electron-phonon coupling under three representative cases, namely, strong, intermediate, and weak local electron-phonon coupling. Figures 3(a)–3(c) correspond to the case of strong local electron-phonon coupling ($|\tau| \ll \lambda$). When ΔV is small, the conductivity σ increases monotonically with increasing ΔV , matching well with the analytical solution in the hopping limit (Appendix B). The Seebeck coefficient α follows the formula for the hopping limit [55]: $\alpha = -\frac{k_B}{e} \ln(\frac{1-c}{c})$, remaining independent of ΔV . Additionally, the mean free path l_{mfp} is much smaller than the lattice constant, suggesting a hopping transport mechanism. Here, mean free path l_{mfp} is defined as [56]

$$l_{\text{mfp}} = \left[\frac{1}{e^2 n_e} C_1(0) \right]^{1/2} \int_0^{+\infty} dt \left| \frac{\text{Re } C_1(t)}{\text{Re } C_1(0)} \right|. \quad (19)$$

When ΔV increases further, σ exhibits a steady rise while moving away from the hopping behavior. Simultaneously, α experiences a decrease due to the widening of the bandwidth, which shall be illustrated in Figs. 4(a) and 4(b). Considering $l_{\text{mfp}} \sim \Omega$, the dominant charge transport mechanism is phonon assisted when ΔV attains large values.

In Figs. 3(g)–3(i), we examine the case of weak local electron-phonon coupling where $\lambda \ll |\tau|$. For small values of ΔV , the conductivity experiences a rapid decrease as ΔV increases, matching well with the predictions of band theory [57]. The Seebeck coefficient matches the constant behavior predicted by band theory (Appendix C) when ΔV is small and exhibits a slight increase as ΔV increases. The observation $l_{\text{mfp}} \gg \Omega$ suggests a bandlike behavior as well. As ΔV increases further, the conductivity continues to decrease, while the Seebeck coefficient starts to decrease due to the broadening of the bandwidth [see Figs. 4(e) and 4(f)]. Considering $l_{\text{mfp}} \sim \Omega$, the transport mechanism conforms to the characteristics of transient localization [58].

In Figs. 3(d)–3(f), we investigate the intermediate case where the transfer integral $|\tau|$ is comparable to the reorganization energy λ . As the parameter ΔV increases, the conductivity exhibits a consistent and monotonic decrease. The Seebeck coefficient, on the other hand, roughly remains

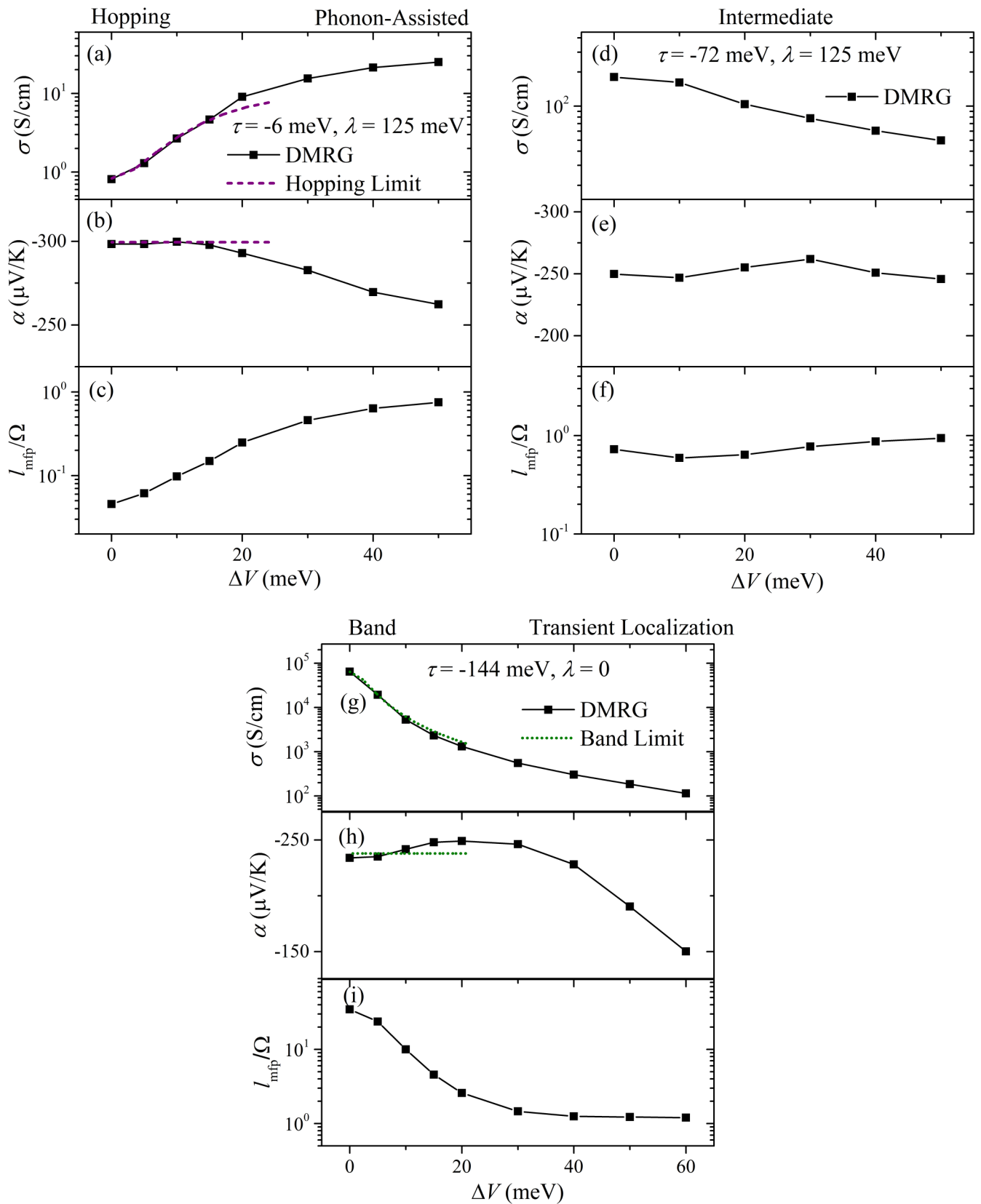


FIG. 3. Influence of nonlocal electron-phonon coupling ΔV on conductivity σ , Seebeck coefficient α , and mean free path l_{mfp} under different local electron-phonon couplings. (a)–(c), (d)–(f), and (g)–(i) correspond to strong, intermediate, and weak local electron-phonon coupling, respectively. Here, $c = 0.03$ and $T = 300$ K.

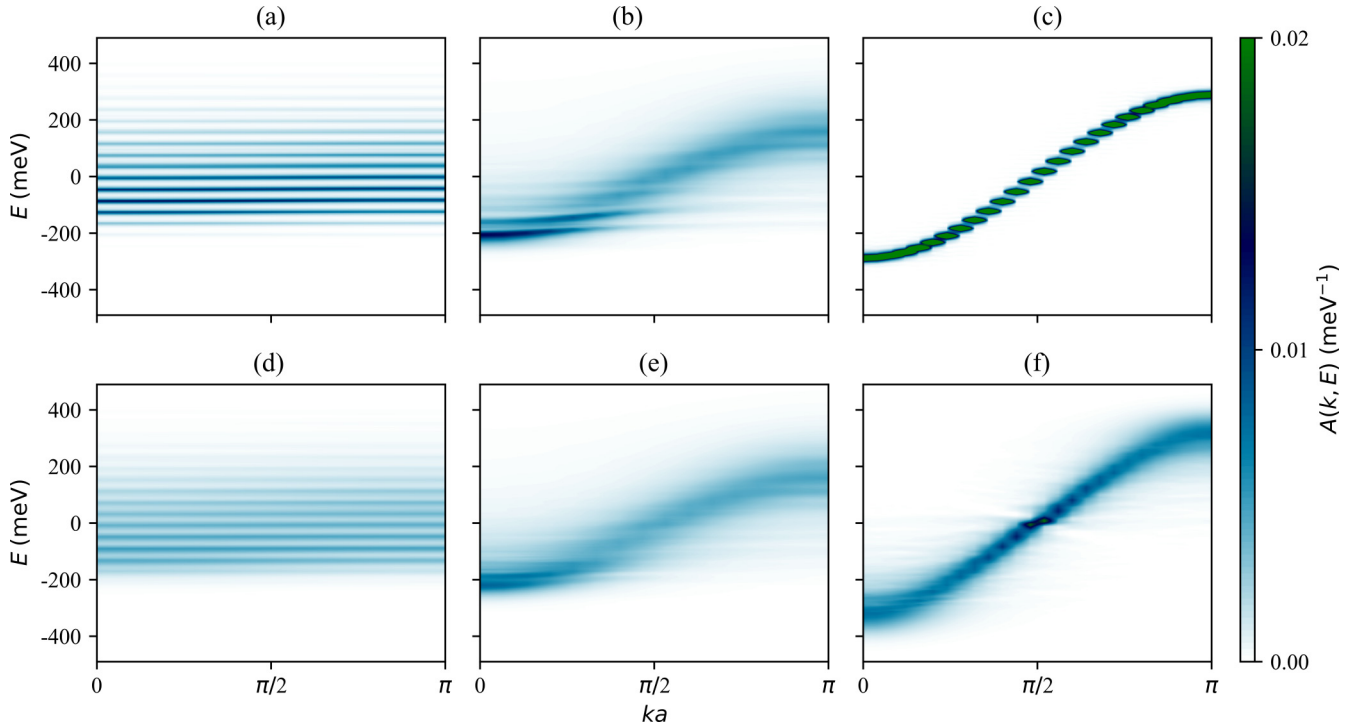


FIG. 4. One-particle spectral density function when $T = 300$ K in (a) hopping regime, (b) intermediate regime 1, (c) band regime, (d) phonon-assisted regime, (e) intermediate regime 2, and (f) transient localization regime.

constant with increasing ΔV . Additionally, l_{mfp} consistently remains comparable to the lattice constant Ω throughout the analysis. These behaviors are different from the mechanism mentioned above and are attributed to the intermediate transport regime [30].

Moreover, it should be noted that, under a different strength of local electron-phonon coupling, the change of ΔV significantly influences the value of conductivity (more than ten times) while it little changes the absolute value of the Seebeck coefficient (less than 10%).

Based on the transport regimes identified in Fig. 3, we select the following representative parameters to cover the five transport regimes mentioned above; specifically, $\tau = -6$ meV, $\lambda = 125$ meV, $g_P = 0.25$ for the hopping regime, $\tau = -6$ meV, $\lambda = 125$ meV, $g_P = 1.5$ for the phonon-assisted regime, $\tau = -72$ meV, $\lambda = 125$ meV, $g_P = 0.25$ and $\tau = -72$ meV, $\lambda = 125$ meV, $g_P = 1.0$ for the intermediate regime (denoted as intermediate regimes 1 and 2), $\tau = -144$ meV, $\lambda = 0$, $g_P = 0.25$ for the band regime, and $\tau = -144$ meV, $\lambda = 0$, $g_P = 2.5$ for the transient localization regime. Note that ΔV is proportional to g_P when the temperature is fixed, and $g_P = 1.0$ corresponds to $\Delta V = 23$ meV when $T = 300$ K. The parameters correspond to the black crosses in Fig. 2.

The influence of nonlocal electron-phonon coupling on the one-particle spectral density function $A(k, E)$ across five transport regimes is plotted in Fig. 4. Here [25],

$$A(k, E) = \frac{1}{N\pi} \sum_{jl} e^{ik\Omega(j-l)} \int_0^{+\infty} \text{Tr}[\hat{a}_j(t)\hat{a}_l^\dagger(0)]e^{iEt} dt. \quad (20)$$

In Fig. 4(a), because of the bandwidth narrowing effect [59] introduced by local coupling, the peaks of each wave number of $A(k, E)$ are very narrow and discrete in the hopping regime, indicating the localization of charge carriers. When nonlocal coupling ΔV grows, the transport behavior comes to the phonon-assisted regime. As presented in Fig. 4(b), $A(k, E)$ becomes more dispersive [36] (the peaks at each wave number are wider). In intermediate regimes 1 and 2 presented in Figs. 4(c) and 4(d), $A(k, E)$ is much wider [i.e., the difference between the peaks of $A(k, E)$ is larger] than Figs. 4(a) and 4(b) because of larger transfer integrals. In the band regime presented in Fig. 4(e), $A(k, E)$ is wide and corresponds to the formula of the energy band, i.e., $E(k) = 2\tau \cos k\Omega$. As the nonlocal coupling increases, the transport mechanism comes to the transient localization regime [30,60], which is shown in Fig. 4(f). Here, $A(k, E)$ is more dispersive than $A(k, E)$ in Fig. 4(e).

The difference between Figs. 4(a) and 4(b), Figs. 4(c) and 4(d), and Figs. 4(e) and 4(f) show that increasing the nonlocal electron-phonon coupling (ΔV) just modifies the shapes of $A(k, E)$ slightly by making $A(k, E)$ more dispersive, while the change of local coupling influences $A(k, E)$ obviously, widening the difference between the peaks, as presented in Figs. 4(a), 4(c), and 4(e). These behaviors are essential as the density of state (DOS) can be calculated as below [25]:

$$D(E) = \frac{1}{V} \sum_k A(k, E). \quad (21)$$

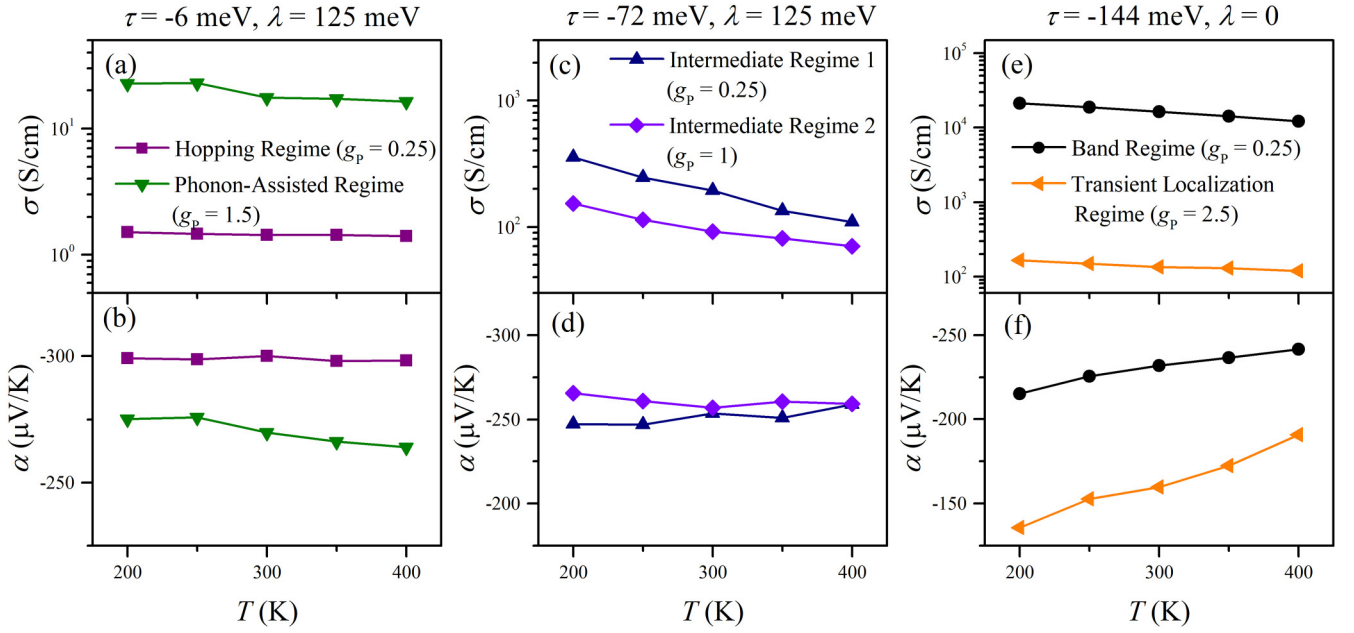


FIG. 5. Temperature dependence of conductivity σ and Seebeck coefficient α in different transport regimes. Here, $c = 0.03$. Note that in (a) and (b) $\tau = -6$ meV and $\lambda = 125$ meV; in (c) and (d) $\tau = -72$ meV and $\lambda = 125$ meV; in (e) and (f) $\tau = -144$ meV and $\lambda = 0$.

According to the general formula for Seebeck coefficients [2],

$$\alpha = \int_{-\infty}^{+\infty} dE \frac{(E - \mu) \sigma(E)}{eT} \left(-\frac{\partial f}{\partial E} \right), \quad (22)$$

where

$$\sigma = \int_{-\infty}^{+\infty} dE \sigma(E) \left(-\frac{\partial f}{\partial E} \right) \quad (23)$$

and

$$\sigma(E) = e\mu_c(E)D(E)k_B T. \quad (24)$$

Here, $f = \frac{1}{1 + \exp(\frac{E - \mu}{k_B T})}$ is the Fermi-Dirac distribution function and $\mu_c(E)$ is the carrier mobility. According to previous research, when the DOS is narrow [18,55], the Seebeck coefficient is a constant $\alpha = -\frac{k_B}{e} \ln(\frac{1-c}{c})$ independent of ΔV , as shown in the hopping regime presented in Fig. 3(b). When the DOS is wide [61], the behavior of the Seebeck coefficient can be qualitatively interpreted via Mott's formula, which indicates that the Seebeck coefficient value is decided by the shape of the DOS, and a wider DOS leads to a lower Seebeck coefficient:

$$\alpha \approx \frac{\pi^2}{3} \frac{k_B}{e} k_B T \left. \frac{d \ln D(E)}{dE} \right|_{E=\mu}. \quad (25)$$

Therefore, (i) the fact that changing the nonlocal coupling (ΔV) just modifies $A(k, E)$ slightly explains why the influence of ΔV only has a small influence on the Seebeck coefficient in Fig. 3 and (ii) the DOS is slightly broadened as ΔV increases when $|\tau| \ll \lambda$ and $|\tau| \gg \lambda$ but remains unchanged as ΔV increases when $|\tau| \sim \lambda$. These explain the decrease of the Seebeck coefficient as ΔV grows in the

phonon-assisted regime [Fig. 3(b)] and the transient localization regime [Fig. 3(h)], and the constant behavior of α in the intermediate regime [Fig. 3(e)].

The temperature dependence of the conductivity and Seebeck coefficient in various transport regimes are depicted in Fig. 5. Specifically, in the hopping regime shown in Figs. 5(a) and 5(b), we observe a decrease in the conductivity with increasing temperature due to the enhancement of the bandwidth narrowing effect. Meanwhile, the Seebeck coefficient remains constant as temperature increases, attributed to the narrow polaron band [18,21]. This behavior aligns with the formula $\alpha = -\frac{k_B}{e} \ln(\frac{1-c}{c})$, which is temperature independent. In the phonon-assisted regime, the conductivity also decreases as temperature rises, while the Seebeck coefficient remains relatively unchanged. In the intermediate transport regime shown in Figs. 5(c) and 5(d), the conductivity experiences a rapid decrease with increasing temperature. Simultaneously, the Seebeck coefficient is roughly independent of temperature. In the transient localization regime and band regime shown in Figs. 5(e) and 5(f), the conductivity decreases with increasing temperature due to the growing dynamic disorder. For the Seebeck coefficient, we observe a roughly linear increase with temperature, which can be interpreted through Mott's formula [61] [Eq. (25)].

Note that the strength of nonlocal electron-phonon coupling ΔV increases as temperature increases [Eq. (7)]. Therefore, the temperature dependence also suggests nonlocal coupling has a significant influence on the electrical conductivity but little effect on the Seebeck coefficient.

Figure 6 illustrates the dependence of transport coefficients on doping ratio c in various transport regimes. Taking electron doping [Figs. 6(a)–6(c)] as an example, we observe that the conductivity consistently increases as the doping ratio

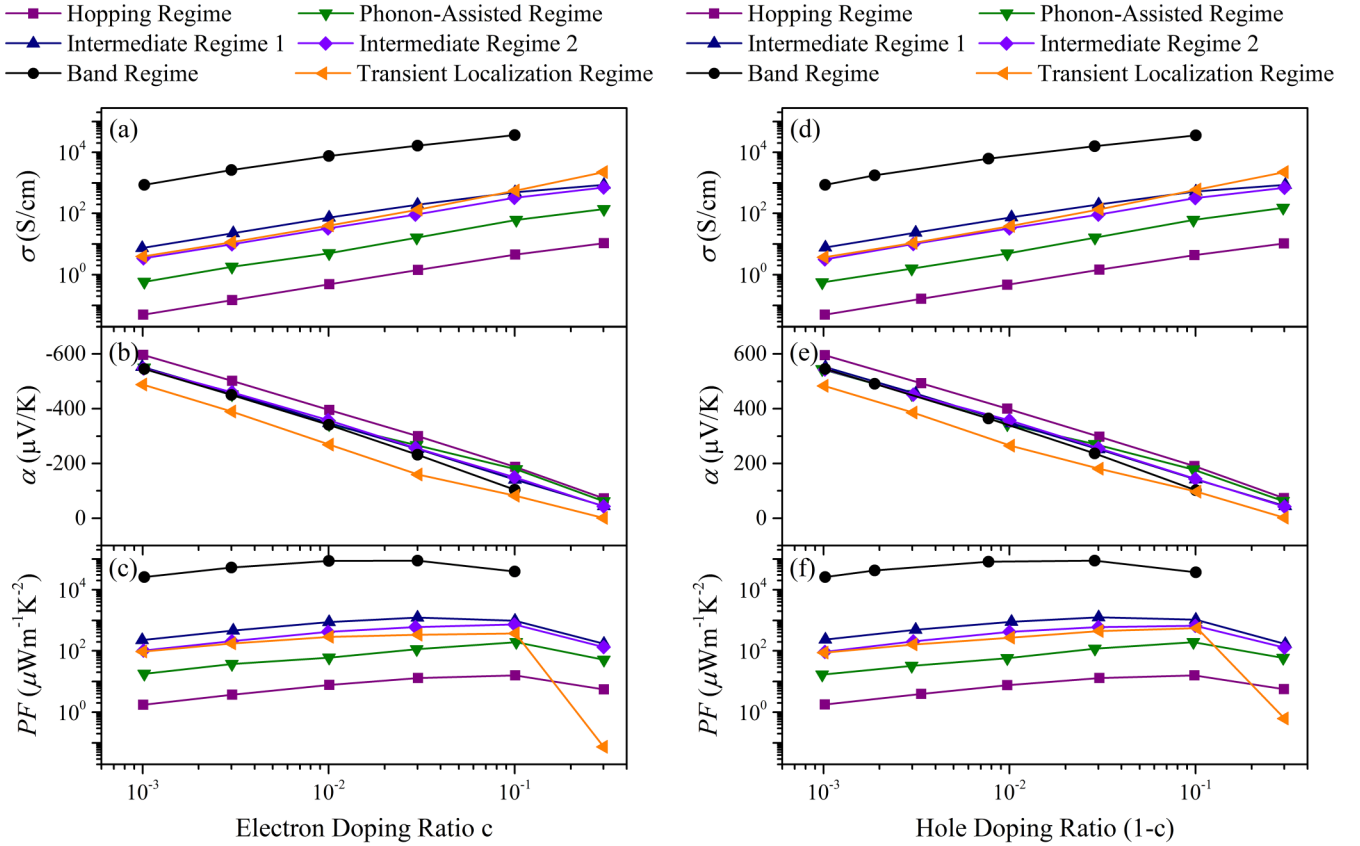


FIG. 6. Dependence of conductivity σ , Seebeck coefficient α , and power factor PF on doping ratio c when $T = 300$ K. (a)–(c) correspond to electron doping and (d)–(f) correspond to hole doping.

increases, while the Seebeck coefficient exhibits an opposite trend. Throughout all transport regimes, the conductivity follows a proportional relationship $\sigma \propto \ln c$, and the Seebeck coefficient roughly follows $\alpha = A \ln c + B$, where A and B are constants. Additionally, the absolute values of conductivity vary significantly across different transport regimes. Typically, we expect higher conductivity in the band regime, intermediate regime, and transient localization regime due to large effective transfer integrals, which are reflected in the spectral density functions shown in Figs. 4(c)–4(f). Different from the huge difference in the value of conductivities in different transport regimes, the values of the Seebeck coefficient are similar in different transport regimes under a fixed doping ratio. Notably, the doping ratio c influences both the conductivity and the Seebeck coefficient significantly, which can be interpreted in Eqs. (22) and (23), where the doping ratio (related to chemical potential μ) is directly involved in the expression of σ and α . The power factors, $PF = \alpha^2 \sigma$, are plotted in Fig. 6(c). The optimal electron doping ratio for achieving the highest power factor is approximately 3%–10% across all transport regimes. Moreover, the case of hole doping is also investigated in Figs. 6(d)–6(f), demonstrating impressive similarities to the electron doping case as expected. It should be noted that the similarities between electron doping and hole doping rely on the validity of the Holstein-Peierls model, which shall fail when electron-electron interactions are significant. For more discussions, see Appendix D.

IV. CONCLUSIONS

In summary, we conducted a comprehensive investigation of the nonlocal electron-phonon coupling's influence on thermoelectric transport in organic materials, adopting the TD-DMRG method that overcomes the limitations of previous approaches. Notably, we find that nonlocal coupling significantly influences conductivity while it has little effect on the Seebeck coefficient, which can be interpreted via the change of DOS and the general expression in thermoelectric transport. Meanwhile, the doping ratio significantly influences both conductivity and the Seebeck coefficient, and when the Holstein-Peierls model is valid, the optimal doping ratio for the highest power factor is making HOMOs (LUMOs) 3%–10% filled by holes (electrons).

Therefore, our work indicates an experimental strategy valid in all transport regimes for higher thermoelectric power factors: we can enhance the conductivity under a specific doping ratio (i.e., mobility) through rational molecular design that enhances the transfer integral or suppresses the strength of the electron-phonon coupling first and then achieve an optimal doping ratio that balances the conductivity and Seebeck coefficient for the highest power factor.

ACKNOWLEDGMENT

This work is supported by the National Natural Science Foundation of China (Grant No. T2350009) and the

TABLE I. Parameters adopted in numerical calculation.

Parameters	Value selection
Virtual bond dimension D	64
Size of local phonon basis d_H	9
Size of nonlocal phonon basis d_P	60
Site number	16
Imaginary time evolution steps	300
Time step Δt of real time evolution	25 a.u. (1 fs = 41.34 a.u.)
Damping function for band regime	$\exp\left[-\left(\frac{t^2}{t_0^2}\right)\right]$, $t_0 = \frac{\hbar}{\gamma_0}$, $\gamma_0 = 2$ meV

Guangdong Provincial Natural Science Foundation (Grant No. 2024A1515011185), as well as the Shenzhen city ‘‘Pengcheng Peacock’’ Talent Program. J.R. is also supported by the National Natural Science Foundation of China via Grant No. 22273005.

APPENDIX A: DETAILS OF NUMERICAL CALCULATIONS

We carry out calculations via the PYTHON package RENORMALIZER. The computational parameters adopted are listed in Table I.

The virtual bond dimension D and the size of nonlocal phonon basis d_P are tested as well, which is plotted in Fig. 7. Note that about 64 is enough for virtual bond dimensions. We suppose the major reason is that the electron fillings adopted in this work are relatively low, which means fewer degenerate states are involved in the calculations. Previous studies [30,46] also support the selection of this relatively small virtual bond dimension. Although relatively small virtual bond dimensions are adopted compared to Hubbard-like models, large physical bond dimensions are selected to ensure an accurate description on vibrations, which is essential in the Holstein-Peierls model and significantly increases computational cost.

In addition, applying \hat{J}_e to $|\Psi_\beta\rangle$ is a main source of truncation error cutoff, which is presented in Table II. We can see that $D = 64$ ensures reasonable error cutoff.

APPENDIX B: HOPPING BEHAVIOR

The conductivity in the hopping limit is calculated via

$$\sigma = n_e e \mu_e, \quad (\text{B1})$$

where electron mobility μ_e is calculated via [30]

$$\mu_e = \frac{e\Omega^2}{k_B T} \int_{-\infty}^{\infty} [\tau^2 + (g_P \omega_P)^2 f(\omega_P, t)] e^{-\Gamma(t)} dt, \quad (\text{B2})$$

$$\Gamma(t) = 2 \sum_n g_{H,n}^2 [1 + 2N(\omega_{H,n}) - f(\omega_{H,n}, t)] + 4g_P^2 [1 + 2N(\omega_P) - f(\omega_P, t)], \quad (\text{B3})$$

TABLE II. Truncation error cutoff of $\hat{J}_e|\Psi_\beta\rangle$. The second column is the truncation error cutoff of $\hat{J}_e|\Psi_\beta\rangle$. (We calculate the truncation error cutoff across every virtual bond and then calculate the average.) The third column is the normalized distance between compressed state $|\Psi_i\rangle$ and reference state $|\Psi_{\text{ref}}\rangle$. Here, we use $D = 192$ as a reference state, and the normalized distance between compressed state $|\Psi_i\rangle$ and reference state $|\Psi_{\text{ref}}\rangle$ is defined as $r_i = 2\| |\Psi_i\rangle - |\Psi_{\text{ref}}\rangle \| / (\| |\Psi_i\rangle \| + \| |\Psi_{\text{ref}}\rangle \|)$. The parameters in intermediate regime 2 are adopted.

Virtual bond dimension of $ \Psi_i\rangle$	$s_i (\times 10^{-4})$	r_i
48	4.30	0.0164
64	2.26	0.0097
96	0.69	0.0041
128	0.30	0.0019

$$f(\omega, t) = (1 + N(\omega))e^{-i\omega t} + N(\omega)e^{i\omega t}, \quad (\text{B4})$$

$$N(\omega) = \frac{1}{e^{\omega/k_B T} - 1}. \quad (\text{B5})$$

The Seebeck coefficient in the hopping limit is calculated via [55]

$$\alpha = -\frac{k_B}{e} \ln\left(\frac{1-c}{c}\right). \quad (\text{B6})$$

APPENDIX C: BAND LIMIT

The band limit in the main text is calculated via the Boltzmann transport equation [57]:

$$\sigma = e^2 \sum_k \left(-\frac{\partial f}{\partial E_k}\right) v_k v_k \theta_k, \quad (\text{C1})$$

$$\alpha = \frac{e}{\sigma} \sum_k \frac{E_k - \mu}{T} \left(-\frac{\partial f}{\partial E_k}\right) v_k v_k \theta_k, \quad (\text{C2})$$

where k is the wave vector, θ_k is the relaxation time, group velocity $v_k = \frac{1}{\hbar} \frac{\partial E_k}{\partial k}$, and f is the Fermi-Dirac distribution function. In rigid band approximation, the energy band of electrons is

$$E_k = 2\tau \cos k\Omega. \quad (\text{C3})$$

The total relaxation time can be expressed as

$$\frac{1}{\theta_{\text{total}}(k)} = \frac{1}{\theta_{\text{imp}}(k)} + \frac{1}{\theta_{\text{ph}}(k)}. \quad (\text{C4})$$

$\theta_{\text{imp}}(k)$ is set as a constant θ_0 which satisfies

$$\sigma(g_P = 0, \lambda = 0) = e^2 \sum_k \left(-\frac{\partial f}{\partial E_k}\right) v_k v_k \theta_0. \quad (\text{C5})$$

According to deformation potential approximation [38],

$$\frac{1}{\theta_{\text{ph}}(k)} = \sum_{k'} \frac{2\pi}{\hbar} \frac{k_B T E_1^2}{C_{ii}} \delta(E_{k'} - E_k) (1 - \cos \gamma). \quad (\text{C6})$$

Here, C_{ii} is the elastic constant, E_1 is the deformation potential constant, and γ is the scattering angle. For a

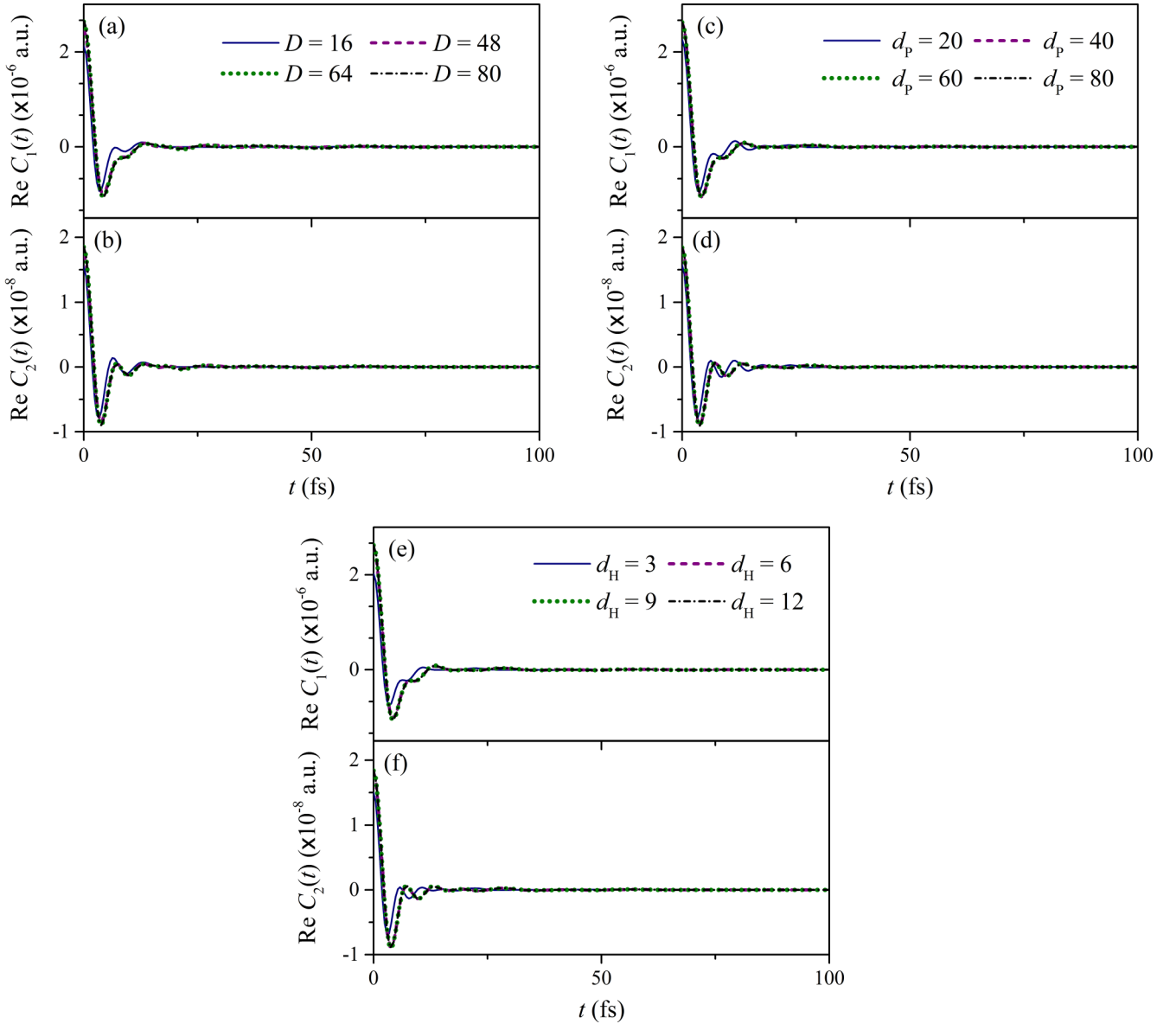


FIG. 7. (a),(b) Convergence of virtual bond dimension D ; (c),(d) convergence of the size of the nonlocal phonon basis d_p ; and (e),(f) convergence of the size of local phonon basis d_H in our work.

one-dimensional system with the $E-k$ relationship presented in Eq. (C3), $\gamma = 0$ or π when $\delta(E_{k'} - E_k)$ is nonzero. Considering the definition of E_1 and C_{ii} , $\frac{1}{\theta_{\text{ph}}(k)}$ is a constant independent of k and proportional to g_P , i.e., $\frac{1}{\theta_{\text{ph}}(k)} = A_g g_P$, where the factor A_g can be calculated by the second data point presented in Fig. 2(g).

APPENDIX D: THE LIMITATION OF HOLSTEIN-PEIERLS MODEL

In this work, we adopted the spinless Holstein-Peierls model. This model is widely used to study the charge transport process in organic materials. However, this model not only ignores Coulombic electron-electron interactions, but also ignores phonon-mediated electron-electron interactions between on-site electrons with different spins. Take the fol-

lowing model as an example:

$$\begin{aligned} \hat{H} = & \sum_{j,\sigma} \epsilon_{j,\sigma} \hat{a}_{j,\sigma}^\dagger \hat{a}_{j,\sigma} + \sum_{jk,\sigma} \tau_{jk} \hat{a}_{j,\sigma}^\dagger \hat{a}_{k,\sigma} \\ & + \sum_{j,n,\sigma} \hbar g_{H,n} \omega_{H,n} (\hat{b}_{jn}^\dagger + \hat{b}_{jn}) \hat{a}_{j,\sigma}^\dagger \hat{a}_{j,\sigma} \\ & + \sum_{j,n} \hbar \omega_{H,n} \left(\hat{b}_{jn}^\dagger \hat{b}_{jn} + \frac{1}{2} \right). \end{aligned} \quad (\text{D1})$$

Here, σ denotes spin up and down. By applying the following unitary transformation,

$$\tilde{H} = e^{\hat{S}} \hat{H} e^{-\hat{S}}, \quad (\text{D2})$$

where

$$\hat{S} = \sum_{j,n,\sigma} g_{H,n} (\hat{b}_{jn}^\dagger - \hat{b}_{jn}) \hat{a}_{j,\sigma}^\dagger \hat{a}_{j,\sigma}. \quad (\text{D3})$$

We will find

$$\begin{aligned} \tilde{H} = & \sum_{j,\sigma} \epsilon_{j,\sigma} \hat{a}_{j,\sigma}^\dagger \hat{a}_{j,\sigma} + \sum_{jk,\sigma} \tau_{jk} \hat{a}_{j,\sigma}^\dagger \hat{a}_{k,\sigma} \hat{X}_j^\dagger \hat{X}_k \\ & + \sum_{j,n} \hbar \omega_{H,n} \left(\hat{b}_{jn}^\dagger \hat{b}_{jn} + \frac{1}{2} \right) - \sum_{j,\sigma} \hbar g_{H,n}^2 \omega_{H,n} \hat{a}_{j,\sigma}^\dagger \hat{a}_{j,\sigma} \\ & - \sum_j 2\hbar g_{H,n}^2 \omega_{H,n} \hat{a}_{j,\uparrow}^\dagger \hat{a}_{j,\uparrow} \hat{a}_{j,\downarrow}^\dagger \hat{a}_{j,\downarrow}, \end{aligned} \quad (\text{D4})$$

where

$$\hat{X}_k = \exp \left[- \sum_n g_{H,n} (\hat{b}_{kn}^\dagger - \hat{b}_{kn}) \right]. \quad (\text{D5})$$

In Eq. (D4), the fifth term corresponds to the influence of phonon-mediated electron-electron coupling. Considering this term is proportional to $\hat{n}_{j,\uparrow} \hat{n}_{j,\downarrow}$, this term is much smaller than other terms when doping ratio c is small. When this term can be ignored, electrons with different spins move independently, and in such case the spinless Holstein-Peierls model is valid. Indeed, in other cases such as heavily doped, the validity of the spinless Holstein-Peierls model should be checked. Moreover, in such cases not only electron-electron Coulomb interactions but also electron-electron interactions mediated by phonons should be taken into account through models such as the Holstein-Hubbard model. We believe both phonon-mediated and Coulombic electron-electron interactions bring interesting physical phenomena, which need to be discussed as a whole in a further study.

-
- [1] S. A. Gregory, R. Hanus, A. Atassi, J. M. Rinehart, J. P. Wooding, A. K. Menon, M. D. Losego, G. J. Snyder, and S. K. Yee, Quantifying charge carrier localization in chemically doped semiconducting polymers, *Nat. Mater.* **20**, 1414 (2021).
- [2] S. Dongmin Kang and G. Jeffrey Snyder, Charge-transport model for conducting polymers, *Nat. Mater.* **16**, 252 (2017).
- [3] X. Shi and J. He, Thermopower and harvesting heat, *Science* **371**, 343 (2021).
- [4] J. He and T. M. Tritt, Advances in thermoelectric materials research: Looking back and moving forward, *Science* **357**, eaak9997 (2017).
- [5] B. Russ, A. Glaudell, J. J. Urban, M. L. Chabynec, and R. A. Segalman, Organic thermoelectric materials for energy harvesting and temperature control, *Nat. Rev. Mater.* **1**, 92 (2016).
- [6] M. Beekman, D. T. Morelli, and G. S. Nolas, Better thermoelectrics through glass-like crystals, *Nat. Mater.* **14**, 1182 (2015).
- [7] O. Bubnova and X. Crispin, Towards polymer-based organic thermoelectric generators, *Energy Environ. Sci.* **5**, 9345 (2012).
- [8] D. Zhou, H. Zhang, H. Zheng, Z. Xu, H. Xu, H. Guo, P. Li, Y. Tong, B. Hu, and L. Chen, Recent advances and prospects of small molecular organic thermoelectric materials, *Small* **18**, e2200679 (2022).
- [9] T. L. D. Tam and J. Xu, Strategies and concepts in n -doped conjugated polymer thermoelectrics, *J. Mater. Chem. A* **9**, 5149 (2021).
- [10] Y. Ge, R. Liu, and Z. Shuai, Abnormal Seebeck effect in doped conducting polymers, *Appl. Phys. Lett.* **118**, 123301 (2021).
- [11] R. Liu, Y. Ge, D. Wang, and Z. Shuai, Understanding the temperature dependence of the Seebeck coefficient from first-principles band structure calculations for organic thermoelectric materials, *CCS Chem.* **3**, 1477 (2021).
- [12] N. Tushima, Conductive polymers as a new type of thermoelectric material, *Macromol. Symp.* **186**, 81 (2002).
- [13] G.-H. Kim, L. Shao, K. Zhang, and K. P. Pipe, Engineered doping of organic semiconductors for enhanced thermoelectric efficiency, *Nat. Mater.* **12**, 719 (2013).
- [14] O. Bubnova, Z. U. Khan, A. Malti, S. Braun, M. Fahlman, M. Berggren, and X. Crispin, Optimization of the thermoelectric figure of merit in the conducting polymer poly(3,4-ethylenedioxythiophene), *Nat. Mater.* **10**, 429 (2011).
- [15] C. Wan, X. Gu, F. Dang, T. Itoh, Y. Wang, H. Sasaki, M. Kondo, K. Koga, K. Yabuki, G. J. Snyder, R. Yang, and K. Koumoto, Flexible n -type thermoelectric materials by organic intercalation of layered transition metal dichalcogenide TiS_2 , *Nat. Mater.* **14**, 622 (2015).
- [16] J. Liu, B. van der Zee, R. Alessandri, S. Sami, J. Dong, M. I. Nugraha, A. J. Barker, S. Rouseva, L. Qiu, X. Qiu, N. Klasan, R. C. Chiechi, D. Baran, M. Caironi, T. D. Anthopoulos, G. Portale, R. W. A. Havenith, S. J. Marrink, J. C. Hummelen, and L. J. A. Koster, N -type organic thermoelectrics: Demonstration of $ZT < 0.3$, *Nat. Commun.* **11**, 5694 (2020).
- [17] E. Selezneva, A. Vercouter, G. Schweicher, V. Lemaury, K. Broch, A. Antidormi, K. Takimiya, V. Coropceanu, J.-L. Brédas, C. Melis, J. Cornil, and H. Siringhaus, Strong suppression of thermal conductivity in the presence of long terminal alkyl chains in low-disorder molecular semiconductors, *Adv. Mater.* **33**, e2008708 (2021).
- [18] D. Emin, *Polarons* (Cambridge University Press, New York, 2013).
- [19] D. Venkateshvaran, M. Nikolka, A. Sadhanala, V. Lemaury, M. Zelazny, M. Kepa, M. Hurhangee, A. J. Kronemeijer, V. Pecunia, I. Nasrallah, I. Romanov, K. Broch, I. McCulloch, D. Emin, Y. Olivier, J. Cornil, D. Beljonne, and H. Siringhaus, Approaching disorder-free transport in high-mobility conjugated polymers, *Nature (London)* **515**, 384 (2014).
- [20] Y. Wang, J. Zhou, and R. Yang, Thermoelectric properties of molecular nanowires, *J. Phys. Chem. C* **115**, 24418 (2011).
- [21] Y.-C. Wang and Y. Zhao, Variational polaron transformation approach toward the calculation of thermopower in organic crystals, *Phys. Rev. B* **101**, 075205 (2020).
- [22] Y. Ge, W. Li, J. Ren, and Z. Shuai, Computational method for evaluating the thermoelectric power factor for organic materials modeled by the Holstein model: A time-dependent density matrix renormalization group formalism, *J. Chem. Theory Comput.* **18**, 6437 (2022).

- [23] A. J. Heeger, Semiconducting and metallic polymers: The fourth generation of polymeric materials, *J. Phys. Chem. B* **105**, 8475 (2001).
- [24] J. L. Bredas and G. B. Street, Polarons, bipolarons, and solitons in conducting polymers, *Acc. Chem. Res.* **18**, 309 (1985).
- [25] J. H. Fetherolf, D. Golež, and T. C. Berkelbach, A unification of the Holstein polaron and dynamic disorder pictures of charge transport in organic crystals, *Phys. Rev. X* **10**, 021062 (2020).
- [26] G. Schweicher, G. D'Avino, M. T. Ruggiero, D. J. Harkin, K. Broch, D. Venkateshvaran, G. Liu, A. Richard, C. Ruzié, J. Armstrong, A. R. Kennedy, K. Shankland, K. Takimiya, Y. H. Geerts, J. A. Zeitler, S. Fratini, and H. Sirringhaus, Chasing the “killer” phonon mode for the rational design of low-disorder, high-mobility molecular semiconductors, *Adv. Mater.* **31**, 1902407 (2019).
- [27] M. Cainelli and Y. Tanimura, Exciton transfer in organic photovoltaic cells: A role of local and nonlocal electron-phonon interactions in a donor domain, *J. Chem. Phys.* **154**, 034107 (2021).
- [28] H.-G. Duan, P. Nalbach, R. J. D. Miller, and M. Thorwart, Ultrafast energy transfer in excitonically coupled molecules induced by a nonlocal Peierls phonon, *J. Phys. Chem. Lett.* **10**, 1206 (2019).
- [29] A. L. Bialas and F. C. Spano, A Holstein–Peierls approach to excimer spectra: The evolution from vibronically structured to unstructured emission, *J. Phys. Chem. C* **126**, 4067 (2022).
- [30] W. Li, J. Ren, and Z. Shuai, A general charge transport picture for organic semiconductors with nonlocal electron-phonon couplings, *Nat. Commun.* **12**, 4260 (2021).
- [31] N. Tessler, Y. Preezant, N. Rappaport, and Y. Roichman, Charge transport in disordered organic materials and its relevance to thin-film devices: A tutorial review, *Adv. Mater.* **21**, 2741 (2009).
- [32] N. Lu, L. Li, and M. Liu, Universal carrier thermoelectric-transport model based on percolation theory in organic semiconductors, *Phys. Rev. B* **91**, 195205 (2015).
- [33] S. Ihnatsenka, X. Crispin, and I. V. Zozoulenko, Understanding hopping transport and thermoelectric properties of conducting polymers, *Phys. Rev. B* **92**, 035201 (2015).
- [34] N. Lu, L. Li, and M. Liu, A review of carrier thermoelectric-transport theory in organic semiconductors, *Phys. Chem. Chem. Phys.* **18**, 19503 (2016).
- [35] R. W. Munn and R. Silbey, Theory of electronic transport in molecular crystals. III. Diffusion coefficient incorporating nonlocal linear electron–phonon coupling, *J. Chem. Phys.* **83**, 1854 (1985).
- [36] R. W. Munn and R. Silbey, Theory of electronic transport in molecular crystals. II. Zeroth order states incorporating nonlocal linear electron–phonon coupling, *J. Chem. Phys.* **83**, 1843 (1985).
- [37] W. Shi, T. Deng, G. Wu, K. Hippalgaonkar, J.-S. Wang, and S.-W. Yang, Unprecedented enhancement of thermoelectric power factor induced by pressure in small-molecule organic semiconductors, *Adv. Mater.* **31**, e1901956 (2019).
- [38] W. Shi, D. Wang, and Z. Shuai, High-performance organic thermoelectric materials: Theoretical insights and computational design, *Adv. Electron. Mater.* **5**, 1800882 (2019).
- [39] X. Gao, K. Uehara, D. D. Klug, S. Patchkovskii, J. S. Tse, and T. M. Tritt, Theoretical studies on the thermopower of semiconductors and low-band-gap crystalline polymers, *Phys. Rev. B* **72**, 125202 (2005).
- [40] A. Troisi, Charge transport in high mobility molecular semiconductors: Classical models and new theories, *Chem. Soc. Rev.* **40**, 2347 (2011).
- [41] A. Troisi and G. Orlandi, Charge-transport regime of crystalline organic semiconductors: Diffusion limited by thermal off-diagonal electronic disorder, *Phys. Rev. Lett.* **96**, 086601 (2006).
- [42] S. Fratini, S. Ciuchi, D. Mayou, G. Trambly de Laissardière, and A. Troisi, A map of high-mobility molecular semiconductors, *Nat. Mater.* **16**, 998 (2017).
- [43] Steven R. White, Density matrix formulation for quantum renormalization groups, *Phys. Rev. Lett.* **69**, 2863 (1992).
- [44] U. Schollwöck, The density-matrix renormalization group in the age of matrix product states, *Ann. Phys.* **326**, 96 (2011).
- [45] S. Paeckel, T. Köhler, A. Swoboda, S. R. Manmana, U. Schollwöck, and C. Hubig, Time-evolution methods for matrix-product states, *Ann. Phys.* **411**, 167998 (2019).
- [46] W. Li, J. Ren, and Z. Shuai, Finite-temperature TD-DMRG for the carrier mobility of organic semiconductors, *J. Phys. Chem. Lett.* **11**, 4930 (2020).
- [47] T. Holstein, Studies of polaron motion: Part II. The “small” polaron, *Ann. Phys.* **281**, 725 (1959).
- [48] T. Nematiram and A. Troisi, Modeling charge transport in high-mobility molecular semiconductors: Balancing electronic structure and quantum dynamics methods with the help of experiments, *J. Chem. Phys.* **152**, 190902 (2020).
- [49] F. Ortman, F. Bechstedt, and K. Hannewald, Theory of charge transport in organic crystals: Beyond Holstein’s small-polaron model, *Phys. Rev. B* **79**, 235206 (2009).
- [50] K. Hannewald and P. A. Bobbert, Anisotropy effects in phonon-assisted charge-carrier transport in organic molecular crystals, *Phys. Rev. B* **69**, 075212 (2004).
- [51] S. Fratini, M. Nikolka, A. Salleo, G. Schweicher, and H. Sirringhaus, Charge transport in high-mobility conjugated polymers and molecular semiconductors, *Nat. Mater.* **19**, 491 (2020).
- [52] V. Coropceanu, R. S. Sánchez-Carrera, P. Paramonov, G. M. Day, and J.-L. Brédas, Interaction of charge carriers with lattice vibrations in organic molecular semiconductors: Naphthalene as a case study, *J. Phys. Chem. C* **113**, 4679 (2009).
- [53] R. S. Sánchez-Carrera, P. Paramonov, G. M. Day, V. Coropceanu, and J.-L. Brédas, Interaction of charge carriers with lattice vibrations in oligoacene crystals from naphthalene to pentacene, *J. Am. Chem. Soc.* **132**, 14437 (2010).
- [54] G. D. Mahan, *Many-Particle Physics*, 3rd ed. (Kluwer Academic/Plenum Publishers, New York, 2000).
- [55] H. Fritzsche, A general expression for the thermoelectric power, *Solid State Commun.* **9**, 1813 (1971).

- [56] N. Prodanović and N. Vukmirović, Charge carrier mobility in systems with local electron-phonon interaction, *Phys. Rev. B* **99**, 104304 (2019).
- [57] D. Wang, W. Shi, J. Chen, J. Xi, and Z. Shuai, Modeling thermoelectric transport in organic materials, *Phys. Chem. Chem. Phys.* **14**, 16505 (2012).
- [58] S. Fratini, D. Mayou, and S. Ciuchi, The transient localization scenario for charge transport in crystalline organic materials, *Adv. Funct. Mater.* **26**, 2292 (2016).
- [59] K. Hannewald, V. M. Stojanović, J. M. T. Schellekens, P. A. Bobbert, G. Kresse, and J. Hafner, Theory of polaron bandwidth narrowing in organic molecular crystals, *Phys. Rev. B* **69**, 075211 (2004).
- [60] S. Fratini and S. Ciuchi, Bandlike motion and mobility saturation in organic molecular semiconductors, *Phys. Rev. Lett.* **103**, 266601 (2009).
- [61] M. Cutler and N. F. Mott, Observation of Anderson localization in an electron gas, *Phys. Rev.* **181**, 1336 (1969).